# The 3D Motorcycle Complex for Structured Volume Decomposition

# — Supplement —

## A. Sparse Serial Motorcycle Complex

Let us expand on the remark in Sec. 4.2 about the alternative of a serial motorcycle complex construction. A proposal in [EGKT08, §7] for the 2D case is to trace motorcycles in a serial rather than simultaneous manner. While this voids canonicity[†], it enables the option to omit tracing motorcycles that would form removable (though not regular-removable) traces right away. For instance, if the two directions neighboring the next motorcycle's direction around a singularity have been traced (out of or into the singularity) already, the motorcycle can be omitted. The result (called *sparse MC* in the following) will be coarser, though not necessarily irreducible.

Following this idea, Alg. A is a modified variant of Alg. 1; the parametrization based Alg. 2 can be modified analogously. The key difference is that fire sources (facets incident at singularities) are processed one after the other, and those that are not necessary to establish a valid configuration around a singularity are skipped. In the loop (line **1**) we prioritize edges that already have some incident burnt facets, and process facets $f$ around an edge $e$ in circular order.

The condition necessary$(e, f)$ (line **2**) is defined as follows. Let $f_{-2}, f_{-1}, f, f_{+1}, f_{+2}$ denote the (possibly cyclically self-overlapping) sequence of facets incident at singular edge $e$ surrounding facet $f$ (in either orientation). Condition necessary$(e, f)$ is true iff either $f_{-1}$ and $f_{+1}$ are not burnt yet, or $f_{-1}$ and $f_{+2}$ are burnt but not $f_{+1}$, or $f_{-2}$ and $f_{+1}$ are burnt but not $f_{-1}$. In these cases $f$ needs to be burnt (i.e., become part of the motorcycle complex as well) as well—otherwise the complex would contain cells with edges with inner angles of 270° (or larger) and would not be a pure cuboid block decomposition.

**Algorithm A:** Serial Motorcycle Complex of Hex Mesh

```
1 foreach singular $e$ and $f \in F_e$ do
2     if necessary$(e, f)$ then $Q$.push$((e, f, 0))$          // ignite
      while $Q$ non-empty do
          $(e, f, d) \leftarrow Q$.pop()
          if alive$(e)$ then // not crossing burnt terrain
              tag $f$                       // mark facet as burnt
              foreach regular interior edge $e' \neq e$ incident to
                $f$ do
                  if opp$(e', f)$ is not tagged then
                    $Q$.push$(e', $opp$(e', f), d+1)$   // spread
  foreach boundary facet $f$ do tag $f$
```

In essence, the algorithm attempts to omit "every other" (to the extent permitted by parity) wall around a singularity right away, rather than achieving this via reduction by wall retraction afterwards. Note that the incorporation of a similar omission strategy directly into the *non-serial* algorithm (as done for the 2D case in [SPGT18, §3.1]) would not be straightforward because the a priori omission decision cannot be made simply per singularity in isolation but would require some form of global coordination in the interconnected network of singular arcs in the 3D case.

The result is a block decomposition that can be expected to be coarser than the immediate result (without reduction by wall retraction) of the algorithms from Sec. 5. Indeed this is the case; however, our proposed *reduced* motorcycle complex typically is even simpler than this sparse serial motorcycle complex, as evident from Tables A and B. Of course reduction could also be applied to the sparse MC, but this yields no consistent benefit (last column).

| **Model** | raw | **MC** | **MC$_s$** | MC$_{rs}$ | $\frac{\text{MC}}{\text{MC}_s}$ | $\frac{\text{MC}}{\text{MC}_{rs}}$ |
|---|---|---|---|---|---|---|
| EXAMPLE 3 | 9087 | 2877 | 5125 | 2691 | 56.1% | 106.9% |
| EXAMPLE 1 | 3137 | 1123 | 1199 | 962 | 93.7% | 116.7% |
| EXAMPLE 2 | 233 | 87 | 280 | 101 | 31.1% | 86.1% |
| DRAGON-HEX | 979 | 357 | 399 | 317 | 89.5% | 112.6 |
| GARGOYLE | 720 | 257 | 283 | 220 | 90.8% | 116.8% |
| ANC101 A1 | 1359 | 460 | 524 | 422 | 87.8% | 109.0% |
| FERTILITY-HEX | 221 | 76 | 80 | 66 | 95.0% | 115.2% |
| PEGASUS-HEX | 1035 | 374 | 408 | 287 | 91.7% | 130.3% |
| KISS HEX | 543 | 200 | 244 | 189 | 82.0% | 105.8% |
| ANC101 | 609 | 207 | 136 | 120 | 152.2% | 172.5% |
| IMPELLER STRESSTEST | 184 | 37 | 71 | 61 | 52.1% | 60.7% |
| ARMADILLO HEX-A | 680 | 266 | 292 | 227 | 91.1% | 117.2% |
| ARMADILLO HEX-B | 396 | 147 | 176 | 133 | 83.5% | 110.5% |
| | | | ⋮ | | | |
| EXAMPLE 5 | 1 | 1 | 1 | 1 | 100.0 | 100.0% |

**Table A:** *Using the dataset from Table 1, reported are the number of blocks in the raw motorcycle complex (raw), fully reduced motorcycle complex (MC), sparse serial motorcycle complex ($MC_s$) and its reduced version ($MC_{rs}$)*

| **Model** | raw | **MC** | **MC$_s$** | MC$_{rs}$ | $\frac{\text{MC}}{\text{MC}_s}$ | $\frac{\text{MC}}{\text{MC}_{rs}}$ |
|---|---|---|---|---|---|---|
| ARMADILLO | 392 | 132 | 207 | 121 | 63.8% | 109.1% |
| BONE | 57 | 15 | 25 | 18 | 60.0% | 83.3% |
| BROKEN BULLET | 25 | 5 | 11 | 9 | 45.5% | 55.6% |
| CAMILLE HAND | 75 | 26 | 42 | 27 | 61.9% | 96.3% |
| CUBE SPHERE | 10 | 4 | 6 | 6 | 66.7% | 66.7% |
| CYLINDER | 11 | 5 | 5 | 5 | 100.0% | 100.0% |
| FANDISK | 43 | 19 | 17 | 14 | 111.8% | 135.7% |
| FANPART | 5 | 3 | 5 | 3 | 60.0% | 100.0% |
| JOINT | 54 | 15 | 21 | 14 | 71.4% | 107.1% |
| KITTEN | 77 | 19 | 53 | 30 | 35.8% | 63.3% |
| PRISMA | 3 | 2 | 2 | 2 | 100.0% | 100.0% |
| ROCKERARM | 217 | 78 | 183 | 114 | 42.6% | 68.4% |
| SCULPTURE | 27 | 13 | 18 | 13 | 72.2% | 100.0% |
| SPHERE | 7 | 2 | 5 | 2 | 40.0% | 100.0% |
| TETRAHEDRON | 4 | 2 | 3 | 2 | 66.7% | 100.0% |

**Table B:** *Using the dataset from Table 2, reported are the number of blocks in the raw motorcycle complex (raw), fully reduced motorcycle complex (MC), sparse serial motorcycle complex ($MC_s$) and its reduced version ($MC_{rs}$)*

---

[†] While the simultaneously constructed 2D motorcycle graph yields a *canonical* decomposition, its serial construction voids this property due to order dependence. For 3D neither algorithm yields a canonical partition, as already the crucial 2D right hand arbitration rule does not extend to 3D.

## B. Constraint System Simplification

We show that, analogous to [MC19, §5.3], the 3D constraint system can be transformed such that only a small subsystem needs to be considered in the exact solver; all other variables are deduced in a back-substitution manner. The subsystem contains only the variables associated with node vertices. This shows that the small system set up in Sec. 6.2.2 is indeed sufficient.

At vertices not incident to any cut or align facets, incident tetrahedra form a single sector and hence, share parametrization values. The equations corresponding to edges incident to such vertices are trivially satisfied and can be left out of the system. This leaves us with a system over the variables of vertices on sheets.

**Cut Sheets.** For each sheet we can denote the parametrization variables of a vertex $p$ in the two sectors on the two sides of the sheet as $\boldsymbol{u}_p^+$ and $\boldsymbol{u}_p^-$. Given a sheet with transition function $\pi$, the transition constraint for an edge $ab$ on the sheet then has the form $\boldsymbol{u}_b^+ - \boldsymbol{u}_a^+ = \pi(\boldsymbol{u}_b^- - \boldsymbol{u}_a^-)$.

Given a sequence of vertices $\boldsymbol{u}_0^\pm, \boldsymbol{u}_1^\pm, \dots, \boldsymbol{u}_n^\pm$ forming a chain of edges on a sheet, the equation corresponding to the $k$-th edge is: $\tau_k^w : \boldsymbol{u}_k^+ - \boldsymbol{u}_{k-1}^+ = \pi(\boldsymbol{u}_k^- - \boldsymbol{u}_{k-1}^-)$.

Cumulative sums of these equations have a simple form, namely

$$\sum_{i=1}^{k} \tau_i^w : \boldsymbol{u}_k^+ - \boldsymbol{u}_0^+ = \pi(\boldsymbol{u}_k^- - \boldsymbol{u}_0^-), \tag{a}$$

All transition constraints of a sheet can hence be rewritten with respect to one selected *base* node vertex of the sheet, with variable $\boldsymbol{u}_0$. Re-ordering the variables in the system such that those corresponding to node sectors come last, the following structure is obtained per sheet:

$$\begin{array}{cccccc|cccccccc}
 & & & & & & & & & & & & \boldsymbol{u}_0^- & \boldsymbol{u}_0^+ \\
\mathbf{1} & & & -\pi & & & & & & & & & -\mathbf{1} & \pi \\
 & \ddots & & & \ddots & & & & & & & & \vdots & \\
 & & \mathbf{1} & & & -\pi & & & & & & & -\mathbf{1} & \pi \\
 & & & & & & \mathbf{1} & & & -\pi & & & -\mathbf{1} & \pi \\
 & & & & & & & \ddots & & & \ddots & & \vdots & \\
 & & & & & & & & \mathbf{1} & & & -\pi & -\mathbf{1} & \pi
\end{array} \tag{b}$$

where each entry is a $3 \times 3$ block ($\pi$: rotational matrix of transition; $\mathbf{1} = \mathrm{diag}(1,1,1)$), because $\boldsymbol{u}$ has three components. The vertical bar separates non-node (left) from node vertex variables (right).

**Align Sheets.** Analogously, cumulative sums of alignment constraints can be built, forming this structure per align sheet:

$$\begin{array}{ccc|cccc}
 & & & & & & \boldsymbol{u}_0 \\
\mathbf{1}^k & & & & & & -\mathbf{1}^k \\
 & \ddots & & & & & \vdots \\
 & & \mathbf{1}^k & & & & -\mathbf{1}^k \\
 & & & \mathbf{1}^k & & & -\mathbf{1}^k \\
 & & & & \ddots & & \vdots \\
 & & & & & \mathbf{1}^k & -\mathbf{1}^k
\end{array} \tag{c}$$

where $\mathbf{1}^k$ is a $1 \times 3$ block: $[1,0,0]$ for $k = 0$, $[0,1,0]$ for $k = 1$, $[0,0,1]$ for $k = 2$, where $k$ is the aligned coordinate component.

**Global System** Combining these systems over all sheets will yield the global system. However, not all non-node vertex variables appear in only one of these systems. It is therefore not evident that the combined system maintains an upper triangular structure among the non-node vertices (the left parts in the above matrices). Concretely, among the non-node vertex variables, those on branches appear in two equations each, because each sector incident on an inner branch vertex is bounded by two sheets. We show that the union of these equations still forms an upper triangular system.

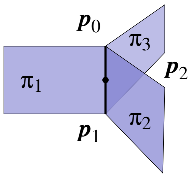

Given a cycle of $n$ sheets incident on a branch with transition functions $\pi_1, \pi_2 \dots \pi_n$ and base node sector variables $\boldsymbol{u}_1^\pm, \boldsymbol{u}_2^\pm \dots \boldsymbol{u}_n^\pm$, respectively, the transition equation for a vertex with sector variables $\boldsymbol{p}_0, \boldsymbol{p}_1 \cdots \boldsymbol{p}_{n-1}$ (see inset figure for n = 3) corresponding to the $k$-th sheet will be: $\boldsymbol{p}_k - \boldsymbol{u}_k^+ = \pi_k(\boldsymbol{p}_{k-1} - \boldsymbol{u}_k^-)$.

Via variable elimination and reordering these can be turned into an upper triangular structure, namely:

$$\begin{array}{cccc|cccccc}
\boldsymbol{p}_1 & \boldsymbol{p}_2 & & \boldsymbol{p}_0 & \boldsymbol{u}_1^- & \boldsymbol{u}_1^+ & & & \boldsymbol{u}_n^- & \boldsymbol{u}_n^+ \\
\mathbf{1} & & & -\pi_1 & \pi_1 & -\mathbf{1} & & & & \\
 & \mathbf{1} & & -\pi_2\pi_1 & \pi_2\pi_1 & -\pi_2 & \pi_2 - \mathbf{1} & & & \\
 & & \ddots & \vdots & \vdots & \vdots & & \ddots & & \\
 & & & \mathbf{1} - \pi_{n\dots}\pi_1 & \pi_{n\dots}\pi_1 & -\pi_{n\dots}\pi_2 & & \dots & \pi_n - \mathbf{1} &
\end{array} \tag{d}$$

In case of a branch lying on the boundary, the sheets around it can be arranged such that the first and last are alignment sheets, i.e., $a_1, \boldsymbol{u}_1^\pm, \boldsymbol{u}_2^\pm \dots \boldsymbol{u}_{n-2}^\pm, a_2$. This yields a lower bidiagonal structure for the non-node variables (easily transformable into triangular form):

$$\begin{array}{cccc|ccccc}
\mathbf{1}^{a_1} & & & & & & & \mathbf{1}^{a_1} & \\
-\pi_1 & \mathbf{1} & & & \pi_1 - \mathbf{1} & & & & \\
 & \ddots & \ddots & & & \ddots & & & \\
 & & -\pi_{n-2} & \mathbf{1} & & & \pi_{n-2} - \mathbf{1} & & \\
 & & & \mathbf{1}^{a_2} & & & & & \mathbf{1}^{a_2}
\end{array} \tag{e}$$

Globally ordering all variables in the system such that those corresponding to node sectors come last, the cumulative transition and alignment equations form the following constraint system:

$$\left[\begin{array}{ccc|c}
A_1 & & & \\
 & A_2 & & B \\
 & & A_3 & \\
\hline
 & 0 & & C
\end{array}\right]$$

where all the sub matrices $A_i$ are upper triangular (formed by the left parts of the above matrices), containing constraints corresponding to, respectively, non-branch sheet vertices (b)+(c), non-node interior branch vertices (d), and non-node boundary branch vertices (e). The small block $C$ is exactly the system we set up and solve in Sec. 6.2.2, and the described simple subsequent propagation process corresponds to back-substitution through $B$ and $A_i$ to the non-node vertex variables.

## C. Complete Version of Table 1

| **Model** | **BC** | BC$^-$ | raw | **MC$^+$** | $\frac{MC^+}{BC}$ | T | **MC** | $\frac{MC}{BC}$ |
|---|---|---|---|---|---|---|---|---|
| 2018 - Fuzzy clustering based pseudo-swept volume decomposition for hexahedral meshing_Example_3 | 406136 | 67828 | 9087 | 5780 | 1.42% | 41.63% | 2877 | 0.71% |
| 2018 - Fuzzy clustering based pseudo-swept volume decomposition for hexahedral meshing_Example_1 | 74331 | 11385 | 3137 | 2248 | 3.02% | 15.09% | 1123 | 1.51% |
| 2018 - Fuzzy clustering based pseudo-swept volume decomposition for hexahedral meshing_Example_2 | 3253 | 678 | 233 | 195 | 5.99% | 13.67% | 87 | 2.67% |
| 2016 - All-Hex Meshing Using Closed-Form Induced Polycube_dragon-hex | 12488 | 2959 | 979 | 724 | 5.8% | 36.33% | 357 | 2.86% |
| 2014 - l1-Based Construction of Polycube Maps from Complex Shapes_gargoyle | 7563 | 1967 | 720 | 546 | 7.22% | 37.62% | 257 | 3.4% |
| 2011 - All-Hex Mesh Generation via Volumetric PolyCube Deformation_anc101_a1 | 12336 | 3118 | 1359 | 846 | 6.86% | 45.33% | 460 | 3.73% |
| 2016 - All-Hex Meshing Using Closed-Form Induced Polycube_fertility-hex | 2002 | 548 | 221 | 189 | 9.44% | 27.02% | 76 | 3.8% |
| 2016 - All-Hex Meshing Using Closed-Form Induced Polycube_pegasus-hex | 9745 | 2415 | 1035 | 729 | 7.48% | 36.29% | 374 | 3.84% |
| 2016 - Efficient Volumetric PolyCube-Map Construction_Kiss_hex | 5019 | 1194 | 543 | 385 | 7.67% | 39.3% | 200 | 3.98% |
| 2014 - l1-Based Construction of Polycube Maps from Complex Shapes_anc101 | 5009 | 1283 | 609 | 347 | 6.93% | 38.9% | 207 | 4.13% |
| 2015 - Practical Hex-Mesh Optimization via Edge-Cone Rectification_impeller_stresstest_in | 878 | 176 | 184 | 124 | 14.12% | 23.86% | 37 | 4.21% |
| 2015 - Practical Hex-Mesh Optimization via Edge-Cone Rectification_impeller_stresstest_out | 878 | 176 | 184 | 124 | 14.12% | 23.86% | 37 | 4.21% |
| 2012 - All-Hex Meshing using Singularity-Restricted Field_impeller | 878 | 182 | 184 | 124 | 14.12% | 23.86% | 39 | 4.44% |
| 2016 - Efficient Volumetric PolyCube-Map Construction_Armadillo_hex-a | 5960 | 1491 | 680 | 516 | 8.66% | 34.19% | 266 | 4.46% |
| 2016 - Efficient Volumetric PolyCube-Map Construction_Armadillo_hex-b | 3265 | 820 | 396 | 296 | 9.07% | 31.45% | 147 | 4.5% |
| 2014 - l1-Based Construction of Polycube Maps from Complex Shapes_dancing-children-2 | 5482 | 1516 | 672 | 533 | 9.72% | 32.9% | 259 | 4.72% |
| 2015 - Practical Hex-Mesh Optimization via Edge-Cone Rectification_dancingchildren_in | 5482 | 1406 | 703 | 546 | 9.96% | 34.52% | 274 | 5% |
| 2015 - Practical Hex-Mesh Optimization via Edge-Cone Rectification_dancingchildren_out | 5482 | 1406 | 703 | 546 | 9.96% | 34.52% | 274 | 5% |
| 2016 - All-Hex Meshing Using Closed-Form Induced Polycube_chinese-lion-hex | 6235 | 1468 | 818 | 589 | 9.45% | 38.82% | 321 | 5.15% |
| 2016 - Efficient Volumetric PolyCube-Map Construction_Dancing_Children_hex | 4755 | 1181 | 682 | 532 | 11.19% | 31.97% | 247 | 5.19% |
| 2012 - All-Hex Meshing using Singularity-Restricted Field_fertility | 1352 | 342 | 234 | 188 | 13.91% | 29.45% | 72 | 5.33% |
| 2015 - Practical Hex-Mesh Optimization via Edge-Cone Rectification_armadillo_in | 2112 | 348 | 308 | 265 | 12.55% | 24.53% | 114 | 5.4% |
| 2015 - Practical Hex-Mesh Optimization via Edge-Cone Rectification_armadillo_out | 2112 | 348 | 308 | 265 | 12.55% | 24.53% | 114 | 5.4% |
| 2015 - Practical Hex-Mesh Optimization via Edge-Cone Rectification_armadillo_stresstest_in | 2112 | 348 | 308 | 265 | 12.55% | 24.53% | 114 | 5.4% |
| 2015 - Practical Hex-Mesh Optimization via Edge-Cone Rectification_armadillo_stresstest_out | 2112 | 348 | 308 | 265 | 12.55% | 24.53% | 114 | 5.4% |
| 2014 - l1-Based Construction of Polycube Maps from Complex Shapes_cognit | 5194 | 1350 | 759 | 574 | 11.05% | 32.35% | 298 | 5.74% |
| 2016 - Efficient Volumetric PolyCube-Map Construction_Dragon_hex | 3655 | 853 | 569 | 442 | 12.09% | 28.81% | 212 | 5.8% |
| 2014 - l1-Based Construction of Polycube Maps from Complex Shapes_elephant | 2842 | 692 | 415 | 346 | 12.17% | 28.97% | 167 | 5.88% |
| 2016 - Efficient Volumetric PolyCube-Map Construction_Elephant_hex | 3105 | 770 | 527 | 399 | 12.85% | 29.15% | 189 | 6.09% |
| 2016 - Efficient Volumetric PolyCube-Map Construction_Bunny_hex | 1282 | 348 | 257 | 187 | 14.59% | 30.74% | 80 | 6.24% |
| 2011 - All-Hex Mesh Generation via Volumetric PolyCube Deformation_Kiss_hex_coarse | 3690 | 1023 | 557 | 402 | 10.89% | 38.44% | 231 | 6.26% |
| 2015 - Practical Hex-Mesh Optimization via Edge-Cone Rectification_dragon_in | 2019 | 495 | 340 | 220 | 10.9% | 27.43% | 127 | 6.29% |
| 2015 - Practical Hex-Mesh Optimization via Edge-Cone Rectification_dragon_out | 2019 | 495 | 340 | 220 | 10.9% | 27.43% | 127 | 6.29% |
| 2011 - All-Hex Mesh Generation via Volumetric PolyCube Deformation_casting | 2805 | 701 | 524 | 409 | 14.58% | 29.47% | 185 | 6.6% |
| 2011 - All-Hex Mesh Generation via Volumetric PolyCube Deformation_kiss_hex | 3690 | 1075 | 688 | 434 | 11.76% | 39.25% | 255 | 6.91% |
| 2016 - Polycube simplification for coarse layouts of surfaces and volumes_chinese_dragon_polycube_in | 810 | 189 | 174 | 147 | 18.15% | 22.66% | 56 | 6.91% |
| 2016 - All-Hex Meshing Using Closed-Form Induced Polycube_grayloc-hex | 3183 | 804 | 604 | 477 | 14.99% | 27.97% | 222 | 6.97% |
| 2013 - PolyCut - Monotone Graph-Cuts for PolyCube Base-Complex Construction_carter_hex_opt | 2500 | 635 | 537 | 410 | 16.4% | 33.74% | 182 | 7.28% |
| 2011 - All-Hex Mesh Generation via Volumetric PolyCube Deformation_Stab3_refine3 | 2227 | 580 | 419 | 290 | 13.02% | 36.08% | 163 | 7.32% |
| 2011 - All-Hex Mesh Generation via Volumetric PolyCube Deformation_bunny_hex | 1324 | 373 | 275 | 194 | 14.65% | 31.87% | 97 | 7.33% |
| 2016 - Polycube simplification for coarse layouts of surfaces and volumes_rockerarm_model_in | 678 | 152 | 162 | 130 | 19.17% | 25.86% | 50 | 7.37% |
| 2016 - Polycube simplification for coarse layouts of surfaces and volumes_rockerarm_polycube_in | 678 | 152 | 162 | 130 | 19.17% | 25.86% | 50 | 7.37% |
| 2017 - A global approach to multi-axis swept mesh generation_Example_4 | 1360 | 324 | 302 | 201 | 14.78% | 24.19% | 101 | 7.43% |
| 2014 - l1-Based Construction of Polycube Maps from Complex Shapes_dragon | 3977 | 998 | 836 | 661 | 16.62% | 28.78% | 301 | 7.57% |
| 2016 - All-Hex Meshing Using Closed-Form Induced Polycube_rockerarm-hex | 1202 | 306 | 223 | 181 | 15.06% | 28.03% | 91 | 7.57% |
| 2017 - A global approach to multi-axis swept mesh generation_Example_1 | 1037 | 243 | 225 | 150 | 14.46% | 22.32% | 81 | 7.81% |
| 2016 - Efficient Volumetric PolyCube-Map Construction_Buste_hex | 1081 | 275 | 244 | 182 | 16.84% | 32.4% | 85 | 7.86% |
| 2016 - Efficient Volumetric PolyCube-Map Construction_Greek_Sculpture_hex | 1476 | 315 | 310 | 244 | 16.53% | 28.44% | 118 | 7.99% |
| 2019 - Singularity Structure Simplification of Hexahedral Mesh via Weighted Ranking_deckel_input | 53116 | 12557 | 10922 | 8823 | 16.61% | 33.39% | 4249 | 8% |
| 2016 - Polycube simplification for coarse layouts of surfaces and volumes_bunny_model_in | 637 | 141 | 151 | 124 | 19.47% | 26.89% | 51 | 8.01% |
| 2016 - Polycube simplification for coarse layouts of surfaces and volumes_bunny_polycube_in | 637 | 141 | 151 | 124 | 19.47% | 26.89% | 51 | 8.01% |
| 2016 - Efficient Volumetric PolyCube-Map Construction_Carter_hex | 2788 | 616 | 630 | 450 | 16.14% | 34.55% | 228 | 8.18% |
| 2013 - PolyCut - Monotone Graph-Cuts for PolyCube Base-Complex Construction_BU_hex_opt | 580 | 141 | 132 | 113 | 19.48% | 27.21% | 48 | 8.28% |
| 2014 - l1-Based Construction of Polycube Maps from Complex Shapes_rockerArm_2 | 835 | 167 | 189 | 149 | 17.84% | 30.57% | 71 | 8.5% |
| 2016 - Efficient Volumetric PolyCube-Map Construction_Bimba_hex-c | 760 | 176 | 204 | 146 | 19.21% | 30.68% | 68 | 8.95% |
| 2012 - All-Hex Meshing using Singularity-Restricted Field_rockerarm | 578 | 135 | 150 | 120 | 20.76% | 30.66% | 52 | 9% |
| 2011 - All-Hex Mesh Generation via Volumetric PolyCube Deformation_bumpy_torus | 2518 | 631 | 595 | 446 | 17.71% | 32.19% | 228 | 9.05% |
| 2011 - All-Hex Mesh Generation via Volumetric PolyCube Deformation_BU_remesh_hex | 1098 | 308 | 301 | 202 | 18.4% | 33.15% | 102 | 9.29% |
| 2017 - A global approach to multi-axis swept mesh generation_Example_3 | 1122 | 280 | 341 | 264 | 23.53% | 18.57% | 105 | 9.36% |
| 2016 - Efficient Volumetric PolyCube-Map Construction_Sphinx_hex-e | 801 | 229 | 222 | 161 | 20.1% | 32.19% | 75 | 9.36% |
| 2016 - Efficient Volumetric PolyCube-Map Construction_Rocker_hex | 730 | 187 | 199 | 156 | 21.37% | 28.02% | 69 | 9.45% |
| 2017 - A global approach to multi-axis swept mesh generation_Example_2 | 974 | 224 | 288 | 202 | 20.74% | 24.89% | 95 | 9.75% |
| 2016 - Polycube simplification for coarse layouts of surfaces and volumes_teapot_model_in | 328 | 68 | 108 | 89 | 27.13% | 28.6% | 32 | 9.76% |
| 2016 - Polycube simplification for coarse layouts of surfaces and volumes_teapot_polycube_in | 328 | 68 | 108 | 89 | 27.13% | 28.6% | 32 | 9.76% |
| 2014 - l1-Based Construction of Polycube Maps from Complex Shapes_bumpy_torus | 2254 | 640 | 592 | 488 | 21.65% | 29.29% | 224 | 9.94% |
| 2013 - PolyCut - Monotone Graph-Cuts for PolyCube Base-Complex Construction_rocker_arm_hex_opt | 664 | 176 | 184 | 138 | 20.78% | 28.81% | 67 | 10.09% |
| 2016 - All-Hex Meshing Using Closed-Form Induced Polycube_kitten-hex | 208 | 57 | 71 | 57 | 27.4% | 24.66% | 21 | 10.1% |
| 2016 - Skeleton-driven Adaptive Hexahedral Meshing of Tubular Shapes_warrior_graded | 4869 | 1306 | 1447 | 1282 | 26.33% | 30.81% | 492 | 10.1% |
| 2019 - Dual Sheet Meshing - An Interactive Approach to Robust Hexahedralization_fandisk.liu18 | 89 | 20 | 35 | 26 | 29.21% | 13.66% | 9 | 10.11% |
| 2014 - l1-Based Construction of Polycube Maps from Complex Shapes_angel_1 | 1284 | 336 | 362 | 266 | 20.72% | 34.99% | 131 | 10.2% |
| 2016 - All-Hex Meshing Using Closed-Form Induced Polycube_carter-hex | 1101 | 235 | 359 | 266 | 24.16% | 35.2% | 114 | 10.35% |
| 2016 - Skeleton-driven Adaptive Hexahedral Meshing of Tubular Shapes_dinopet_graded | 2253 | 617 | 721 | 630 | 27.96% | 32.67% | 234 | 10.39% |
| 2015 - Practical Hex-Mesh Optimization via Edge-Cone Rectification_bust_in | 494 | 102 | 128 | 110 | 22.27% | 27.34% | 52 | 10.53% |
| 2015 - Practical Hex-Mesh Optimization via Edge-Cone Rectification_bust_out | 494 | 102 | 128 | 110 | 22.27% | 27.34% | 52 | 10.53% |
| 2015 - Practical Hex-Mesh Optimization via Edge-Cone Rectification_KingKong_in | 180 | 45 | 71 | 62 | 34.44% | 25% | 19 | 10.56% |
| 2015 - Practical Hex-Mesh Optimization via Edge-Cone Rectification_KingKong_out | 180 | 45 | 71 | 62 | 34.44% | 25% | 19 | 10.56% |
| 2014 - l1-Based Construction of Polycube Maps from Complex Shapes_kiss | 1896 | 567 | 560 | 418 | 22.05% | 32.88% | 205 | 10.81% |
| 2016 - Skeleton-driven Adaptive Hexahedral Meshing of Tubular Shapes_dino_graded | 904 | 275 | 306 | 261 | 28.87% | 33.99% | 99 | 10.95% |
| 2016 - Structured Volume Decomposition via Generalized Sweeping_fertility_1 | 301 | 73 | 119 | 105 | 34.88% | 22.71% | 33 | 10.96% |
| 2019 - Selective Padding for Polycube-Based Hexahedral Meshing_Double_hinge_WH | 153 | 16 | 43 | 43 | 28.1% | 10% | 17 | 11.11% |
| 2016 - Structured Volume Decomposition via Generalized Sweeping_fertility_2 | 301 | 50 | 119 | 105 | 34.88% | 22.71% | 34 | 11.3% |
| 2016 - Structured Volume Decomposition via Generalized Sweeping_fertility_3 | 301 | 71 | 119 | 105 | 34.88% | 22.71% | 34 | 11.3% |
| 2013 - PolyCut - Monotone Graph-Cuts for PolyCube Base-Complex Construction_bunny_hex_opt | 580 | 120 | 170 | 127 | 21.9% | 30.17% | 66 | 11.38% |
| 2016 - Polycube simplification for coarse layouts of surfaces and volumes_asm_model_out | 122 | 33 | 68 | 64 | 52.46% | 14.29% | 14 | 11.48% |
| 2016 - Polycube simplification for coarse layouts of surfaces and volumes_asm_polycube_out | 122 | 33 | 68 | 64 | 52.46% | 14.29% | 14 | 11.48% |
| 2017 - Hexahedral Mesh Generation via Constrained Quadrilateralization_joint | 83 | 18 | 41 | 27 | 32.53% | 15.43% | 10 | 12.05% |
| 2016 - Polycube simplification for coarse layouts of surfaces and volumes_fandisk_polycube_in | 229 | 49 | 89 | 70 | 30.57% | 21.43% | 29 | 12.66% |

**Table C:** *Statistics on a dataset of hexahedral meshes. Numbers of blocks in the base complex (BC), reduced base complex (BC$^-$), raw motorcycle complex (raw), reduced motorcycle complex with preserved singularity-adjacent walls (MC$^+$), fully reduced motorcycle complex (MC), percentage of arcs that are T-arcs (T).*

| **Model** | **BC** | $BC^-$ | raw | **$MC^+$** | $\frac{MC^+}{BC}$ | T | **MC** | $\frac{MC}{BC}$ |
|---|---|---|---|---|---|---|---|---|
| 2014 - L1-Based Construction of Polycube Maps from Complex Shapes_rockerArm_1 | 686 | 183 | 247 | 186 | 27.11% | 27.02% | 87 | 12.68% |
| 2015 - Practical Hex-Mesh Optimization via Edge-Cone Rectification_cap_in | 327 | 97 | 124 | 92 | 28.13% | 34.55% | 42 | 12.84% |
| 2015 - Practical Hex-Mesh Optimization via Edge-Cone Rectification_cap_out | 327 | 97 | 124 | 92 | 28.13% | 34.55% | 42 | 12.84% |
| 2016 - Polycube simplification for coarse layouts of surfaces and volumes_rockerarm_model_out | 316 | 62 | 130 | 116 | 36.71% | 16.14% | 41 | 12.97% |
| 2013 - PolyCut - Monotone Graph-Cuts for PolyCube Base-Complex Construction_fertility_hex_opt | 693 | 153 | 243 | 202 | 29.15% | 25.95% | 91 | 13.13% |
| 2016 - Polycube simplification for coarse layouts of surfaces and volumes_rockerarm_polycube_out | 348 | 60 | 132 | 117 | 33.62% | 19.5% | 46 | 13.22% |
| 2016 - Efficient Volumetric PolyCube-Map Construction_Bimba_hex-d | 196 | 60 | 97 | 63 | 32.14% | 23.77% | 26 | 13.27% |
| 2019 - Selective Padding for Polycube-Based Hexahedral Meshing_Lego_L2 | 525 | 83 | 221 | 167 | 31.81% | 29.6% | 70 | 13.33% |
| 2019 - Dual Sheet Meshing - An Interactive Approach to Robust Hexahedralization_fandisk | 89 | 14 | 36 | 27 | 30.34% | 10.99% | 12 | 13.48% |
| 2016 - Efficient Volumetric PolyCube-Map Construction_Blade_hex | 389 | 90 | 142 | 130 | 33.42% | 20.78% | 53 | 13.62% |
| 2016 - Efficient Volumetric PolyCube-Map Construction_Fertility_hex-largel | 633 | 148 | 244 | 211 | 33.33% | 22.91% | 87 | 13.74% |
| 2016 - Efficient Volumetric PolyCube-Map Construction_Fertility_hex-small | 621 | 158 | 243 | 210 | 33.82% | 23.37% | 87 | 14.01% |
| 2019 - Singularity Structure Simplification of Hexahedral Mesh via Weighted Ranking_fertility_input | 20840 | 5523 | 8344 | 7105 | 34.09% | 30.4% | 2951 | 14.16% |
| 2014 - L1-Based Construction of Polycube Maps from Complex Shapes_angel_2 | 302 | 75 | 116 | 103 | 34.11% | 23.08% | 43 | 14.24% |
| 2019 - Selective Padding for Polycube-Based Hexahedral Meshing_Double_hinge_NH | 105 | 15 | 35 | 35 | 33.33% | 6.67% | 15 | 14.29% |
| 2016 - Polycube simplification for coarse layouts of surfaces and volumes_table1_polycube_in | 195 | 42 | 93 | 80 | 41.03% | 25.17% | 28 | 14.36% |
| 2011 - All-Hex Mesh Generation via Volumetric PolyCube Deformation_fertility_refine | 598 | 161 | 243 | 209 | 34.95% | 24.86% | 87 | 14.55% |
| 2014 - L1-Based Construction of Polycube Maps from Complex Shapes_canewt | 879 | 243 | 357 | 270 | 30.72% | 30.87% | 128 | 14.56% |
| 2019 - Dual Sheet Meshing - An Interactive Approach to Robust Hexahedralization_hanger | 41 | 11 | 30 | 20 | 48.78% | 15.33% | 6 | 14.63% |
| 2019 - Singularity Structure Simplification of Hexahedral Mesh via Weighted Ranking_buste_input | 18355 | 4925 | 7667 | 6570 | 35.79% | 30.83% | 2722 | 14.83% |
| 2012 - All-Hex Meshing using Singularity-Restricted Field_bunny | 259 | 52 | 101 | 93 | 35.91% | 19.65% | 39 | 15.06% |
| 2019 - Selective Padding for Polycube-Based Hexahedral Meshing_Joint | 119 | 17 | 42 | 33 | 27.73% | 12.92% | 18 | 15.13% |
| 2012 - All-Hex Meshing using Singularity-Restricted Field_rod | 66 | 9 | 37 | 27 | 40.91% | 18.09% | 10 | 15.15% |
| 2019 - Dual Sheet Meshing - An Interactive Approach to Robust Hexahedralization_joint | 59 | 10 | 33 | 24 | 40.68% | 10.37% | 9 | 15.25% |
| 2016 - All-Hex Meshing Using Closed-Form Induced Polycube_hollow-eight-hex | 249 | 61 | 108 | 76 | 30.52% | 39.2% | 38 | 15.26% |
| 2019 - Singularity Structure Simplification of Hexahedral Mesh via Weighted Ranking_buste_output | 190 | 45 | 90 | 82 | 43.16% | 17.75% | 29 | 15.26% |
| 2016 - Structured Volume Decomposition via Generalized Sweeping_cat_2_padded | 19 | 3 | 19 | 14 | 73.68% | 23.29% | 3 | 15.79% |
| 2016 - Structured Volume Decomposition via Generalized Sweeping_Dolphin_padded | 19 | 3 | 19 | 14 | 73.68% | 23.29% | 3 | 15.79% |
| 2016 - Structured Volume Decomposition via Generalized Sweeping_femur1_padded | 19 | 3 | 19 | 14 | 73.68% | 23.29% | 3 | 15.79% |
| 2016 - Structured Volume Decomposition via Generalized Sweeping_rabbit_padded | 19 | 3 | 19 | 14 | 73.68% | 23.29% | 3 | 15.79% |
| 2016 - Structured Volume Decomposition via Generalized Sweeping_rotellipse_padded | 19 | 3 | 19 | 14 | 73.68% | 23.29% | 3 | 15.79% |
| 2016 - Polycube simplification for coarse layouts of surfaces and volumes_asm_model_in | 200 | 52 | 80 | 66 | 33% | 23.08% | 32 | 16% |
| 2016 - Polycube simplification for coarse layouts of surfaces and volumes_asm_polycube_in | 200 | 52 | 80 | 66 | 33% | 23.08% | 32 | 16% |
| 2019 - Selective Padding for Polycube-Based Hexahedral Meshing_Bearing | 184 | 46 | 70 | 64 | 34.78% | 12.73% | 30 | 16.3% |
| 2016 - Polycube simplification for coarse layouts of surfaces and volumes_femur_model_out | 110 | 29 | 57 | 55 | 50% | 16.48% | 18 | 16.36% |
| 2014 - L1-Based Construction of Polycube Maps from Complex Shapes_fertility | 460 | 124 | 212 | 188 | 40.87% | 20.33% | 76 | 16.52% |
| 2019 - Singularity Structure Simplification of Hexahedral Mesh via Weighted Ranking_pig_output | 876 | 202 | 420 | 339 | 38.7% | 28.33% | 146 | 16.67% |
| 2016 - All-Hex Meshing Using Closed-Form Induced Polycube_joint-hex | 59 | 10 | 31 | 22 | 37.29% | 15.72% | 10 | 16.95% |
| 2016 - Polycube simplification for coarse layouts of surfaces and volumes_cubespikes_model_in | 276 | 53 | 123 | 105 | 38.04% | 21.02% | 47 | 17.03% |
| 2016 - Polycube simplification for coarse layouts of surfaces and volumes_cubespikes_polycube_in | 276 | 53 | 123 | 105 | 38.04% | 21.02% | 47 | 17.03% |
| 2012 - All-Hex Meshing using Singularity-Restricted Field_ellipsoid-A | 34 | 7 | 27 | 14 | 41.18% | 32.18% | 6 | 17.65% |
| 2019 - Singularity Structure Simplification of Hexahedral Mesh via Weighted Ranking_bottle2_output | 318 | 73 | 175 | 157 | 49.37% | 18.26% | 57 | 17.92% |
| 2012 - All-Hex Meshing using Singularity-Restricted Field_hanger | 50 | 7 | 27 | 22 | 44% | 16.08% | 9 | 18% |
| 2012 - All-Hex Meshing using Singularity-Restricted Field_joint | 83 | 21 | 47 | 28 | 33.73% | 17.8% | 15 | 18.07% |
| 2017 - Hexahedral Mesh Generation via Constrained Quadrilateralization_pone.0177603.s003 | 83 | 21 | 47 | 28 | 33.73% | 17.8% | 15 | 18.07% |
| 2019 - Singularity Structure Simplification of Hexahedral Mesh via Weighted Ranking_toy2_input | 14288 | 3857 | 7161 | 6153 | 43.06% | 30.76% | 2585 | 18.09% |
| 2016 - Polycube simplification for coarse layouts of surfaces and volumes_table1_polycube_out | 149 | 31 | 86 | 72 | 48.32% | 25.77% | 27 | 18.12% |
| 2016 - Polycube simplification for coarse layouts of surfaces and volumes_fandisk_polycube_out | 160 | 46 | 79 | 67 | 41.88% | 18.01% | 29 | 18.13% |
| 2019 - Singularity Structure Simplification of Hexahedral Mesh via Weighted Ranking_toy1_input | 18883 | 5246 | 9461 | 8122 | 43.01% | 29.98% | 3427 | 18.15% |
| 2016 - Polycube simplification for coarse layouts of surfaces and volumes_femur_polycube_out | 110 | 30 | 57 | 55 | 50% | 16.48% | 20 | 18.18% |
| 2016 - Polycube simplification for coarse layouts of surfaces and volumes_bunny_model_out | 197 | 53 | 109 | 99 | 50.25% | 13.94% | 36 | 18.27% |
| 2016 - Polycube simplification for coarse layouts of surfaces and volumes_bunny_polycube_out | 197 | 53 | 109 | 99 | 50.25% | 13.94% | 36 | 18.27% |
| 2012 - All-Hex Meshing using Singularity-Restricted Field_fandisk | 49 | 11 | 25 | 22 | 44.9% | 11.61% | 9 | 18.37% |
| 2017 - Hexahedral Mesh Generation via Constrained Quadrilateralization_fandisk | 49 | 11 | 28 | 22 | 44.9% | 11.61% | 9 | 18.37% |
| 2017 - Hexahedral Mesh Generation via Constrained Quadrilateralization_pone.0177603.s002 | 49 | 16 | 27 | 22 | 44.9% | 11.61% | 9 | 18.37% |
| 2019 - Dual Sheet Meshing - An Interactive Approach to Robust Hexahedralization_rockarm | 119 | 35 | 59 | 41 | 34.45% | 18.12% | 22 | 18.49% |
| 2016 - Polycube simplification for coarse layouts of surfaces and volumes_hand_model_in | 172 | 35 | 81 | 77 | 44.77% | 17.77% | 32 | 18.6% |
| 2016 - Polycube simplification for coarse layouts of surfaces and volumes_hand_polycube_in | 172 | 35 | 81 | 77 | 44.77% | 17.77% | 32 | 18.6% |
| 2019 - Singularity Structure Simplification of Hexahedral Mesh via Weighted Ranking_pig_input | 13987 | 3768 | 7144 | 6078 | 43.45% | 30.98% | 2610 | 18.66% |
| 2019 - Singularity Structure Simplification of Hexahedral Mesh via Weighted Ranking_bottle2_input | 35860 | 9968 | 19360 | 16349 | 45.59% | 31.63% | 6816 | 19.01% |
| 2016 - Structured Volume Decomposition via Generalized Sweeping_kitten_with_bifur_2 | 26 | 8 | 22 | 22 | 84.62% | 10.53% | 5 | 19.23% |
| 2019 - Singularity Structure Simplification of Hexahedral Mesh via Weighted Ranking_deckel_output | 806 | 237 | 450 | 382 | 47.39% | 24.24% | 155 | 19.23% |
| 2016 - Polycube simplification for coarse layouts of surfaces and volumes_femur_model_in | 145 | 36 | 63 | 59 | 40.69% | 21.74% | 28 | 19.31% |
| 2016 - Polycube simplification for coarse layouts of surfaces and volumes_femur_polycube_in | 145 | 36 | 63 | 59 | 40.69% | 21.74% | 28 | 19.31% |
| 2016 - Structured Volume Decomposition via Generalized Sweeping_rockerarm_3 | 82 | 16 | 57 | 53 | 64.63% | 22.83% | 16 | 19.51% |
| 2012 - All-Hex Meshing using Singularity-Restricted Field_sculpture-A | 51 | 11 | 27 | 21 | 41.18% | 12.86% | 10 | 19.61% |
| 2011 - All-Hex Mesh Generation via Volumetric PolyCube Deformation_asm001 | 122 | 28 | 68 | 64 | 52.46% | 14.29% | 24 | 19.67% |
| 2014 - L1-Based Construction of Polycube Maps from Complex Shapes_rod | 122 | 30 | 70 | 64 | 52.46% | 14.29% | 24 | 19.67% |
| 2017 - Explicit Cylindrical Maps for General Tubular Shapes_cactus | 81 | 21 | 57 | 51 | 62.96% | 21.54% | 16 | 19.75% |
| 2014 - L1-Based Construction of Polycube Maps from Complex Shapes_buste | 361 | 99 | 203 | 166 | 45.98% | 21.07% | 72 | 19.94% |
| 2015 - Practical Hex-Mesh Optimization via Edge-Cone Rectification_hanger_stresstest_in | 50 | 10 | 28 | 21 | 42% | 15.94% | 10 | 20% |
| 2015 - Practical Hex-Mesh Optimization via Edge-Cone Rectification_hanger_stresstest_out | 50 | 10 | 28 | 21 | 42% | 15.94% | 10 | 20% |
| 2016 - Polycube simplification for coarse layouts of surfaces and volumes_chinese_dragon_polycube_out | 295 | 70 | 151 | 132 | 44.75% | 18.73% | 59 | 20% |
| 2016 - Polycube simplification for coarse layouts of surfaces and volumes_teapot_model_out | 193 | 43 | 98 | 88 | 45.6% | 21.76% | 39 | 20.21% |
| 2016 - Polycube simplification for coarse layouts of surfaces and volumes_teapot_polycube_out | 193 | 43 | 98 | 88 | 45.6% | 21.76% | 39 | 20.21% |
| 2016 - Polycube simplification for coarse layouts of surfaces and volumes_block_model_in | 162 | 42 | 109 | 105 | 64.81% | 8.66% | 33 | 20.37% |
| 2016 - Polycube simplification for coarse layouts of surfaces and volumes_block_polycube_in | 162 | 42 | 109 | 105 | 64.81% | 8.66% | 33 | 20.37% |
| 2019 - Selective Padding for Polycube-Based Hexahedral Meshing_Lego_L0 | 983 | 236 | 627 | 604 | 61.44% | 13.82% | 205 | 20.85% |
| 2019 - Singularity Structure Simplification of Hexahedral Mesh via Weighted Ranking_eight_input | 3867 | 1076 | 2250 | 1963 | 50.76% | 24.04% | 813 | 21.02% |
| 2016 - Structured Volume Decomposition via Generalized Sweeping_twistedu | 19 | 4 | 19 | 14 | 73.68% | 23.29% | 4 | 21.05% |
| 2016 - Skeleton-driven Adaptive Hexahedral Meshing of Tubular Shapes_armadillo | 301 | 82 | 180 | 165 | 54.82% | 7.49% | 64 | 21.26% |
| 2014 - L1-Based Construction of Polycube Maps from Complex Shapes_bunny | 273 | 73 | 157 | 129 | 47.25% | 21.89% | 59 | 21.61% |
| 2015 - Practical Hex-Mesh Optimization via Edge-Cone Rectification_bunny_in | 273 | 74 | 153 | 128 | 46.89% | 20.42% | 59 | 21.61% |
| 2015 - Practical Hex-Mesh Optimization via Edge-Cone Rectification_bunny_out | 273 | 74 | 153 | 128 | 46.89% | 20.42% | 59 | 21.61% |
| 2012 - All-Hex Meshing using Singularity-Restricted Field_bone | 87 | 15 | 50 | 43 | 49.43% | 29.27% | 19 | 21.84% |
| 2019 - Singularity Structure Simplification of Hexahedral Mesh via Weighted Ranking_fertility_output | 310 | 99 | 222 | 220 | 70.97% | 6.93% | 68 | 21.94% |
| 2016 - Polycube simplification for coarse layouts of surfaces and volumes_table2_polycube_in | 90 | 26 | 61 | 56 | 62.22% | 11.51% | 20 | 22.22% |

**Table C:** *Statistics on a dataset of hexahedral meshes. Numbers of blocks in the base complex (BC), reduced base complex ($BC^-$), raw motorcycle complex (raw), reduced motorcycle complex with preserved singularity-adjacent walls ($MC^+$), fully reduced motorcycle complex (MC), percentage of arcs that are T-arcs (T).*

| **Model** | **BC** | $BC^-$ | raw | $\mathbf{MC^+}$ | $\frac{MC^+}{BC}$ | T | **MC** | $\frac{MC}{BC}$ |
|---|---|---|---|---|---|---|---|---|
| 2019 - Selective Padding for Polycube-Based Hexahedral Meshing_Chamfer_L4 | 22 | 5 | 11 | 11 | 50% | 6.02% | 5 | 22.73% |
| 2014 - l1-Based Construction of Polycube Maps from Complex Shapes_kitty | 121 | 28 | 68 | 59 | 48.76% | 23.13% | 28 | 23.14% |
| 2016 - Structured Volume Decomposition via Generalized Sweeping_rockerarm_2 | 82 | 17 | 57 | 53 | 64.63% | 22.83% | 19 | 23.17% |
| 2019 - Singularity Structure Simplification of Hexahedral Mesh via Weighted Ranking_eight_output | 43 | 6 | 35 | 35 | 81.4% | 15% | 10 | 23.26% |
| 2016 - Structured Volume Decomposition via Generalized Sweeping_Kitten_with_bifur_padded | 82 | 16 | 57 | 53 | 64.63% | 22.83% | 20 | 24.39% |
| 2016 - Structured Volume Decomposition via Generalized Sweeping_rockerarm_1 | 82 | 18 | 57 | 53 | 64.63% | 22.83% | 20 | 24.39% |
| 2016 - Structured Volume Decomposition via Generalized Sweeping_hand7_padded | 159 | 36 | 102 | 91 | 57.23% | 23.29% | 39 | 24.53% |
| 2019 - Selective Padding for Polycube-Based Hexahedral Meshing_Wrench | 61 | 13 | 32 | 30 | 49.18% | 6.48% | 15 | 24.59% |
| 2012 - All-Hex Meshing using Singularity-Restricted Field_sculpture-B | 69 | 16 | 33 | 33 | 47.83% | 10.17% | 17 | 24.64% |
| 2019 - Singularity Structure Simplification of Hexahedral Mesh via Weighted Ranking_toy1_output | 144 | 35 | 113 | 104 | 72.22% | 11.09% | 36 | 25% |
| 2019 - Dual Sheet Meshing - An Interactive Approach to Robust Hexahedralization_bunny | 34 | 7 | 20 | 17 | 50% | 8.89% | 9 | 26.47% |
| 2016 - Skeleton-driven Adaptive Hexahedral Meshing of Tubular Shapes_dinopet | 117 | 31 | 113 | 109 | 93.16% | 5.98% | 31 | 26.5% |
| 2016 - Skeleton-driven Adaptive Hexahedral Meshing of Tubular Shapes_big_buddy | 124 | 36 | 101 | 88 | 70.97% | 10.89% | 33 | 26.61% |
| 2016 - Skeleton-driven Adaptive Hexahedral Meshing of Tubular Shapes_rocker_arm | 45 | 13 | 39 | 39 | 86.67% | 10.34% | 12 | 26.67% |
| 2019 - Selective Padding for Polycube-Based Hexahedral Meshing_Chamfer_L0 | 29 | 8 | 18 | 18 | 62.07% | 2.48% | 8 | 27.59% |
| 2016 - All-Hex Meshing Using Closed-Form Induced Polycube_knot-hex | 50 | 16 | 40 | 40 | 80% | 15.79% | 14 | 28% |
| 2014 - l1-Based Construction of Polycube Maps from Complex Shapes_angel_3 | 78 | 22 | 64 | 54 | 69.23% | 17.8% | 22 | 28.21% |
| 2012 - All-Hex Meshing using Singularity-Restricted Field_ellipsoid-B | 7 | 2 | 7 | 7 | 100% | 0% | 2 | 28.57% |
| 2012 - All-Hex Meshing using Singularity-Restricted Field_ellipsoid-C | 7 | 2 | 7 | 7 | 100% | 0% | 2 | 28.57% |
| 2016 - Skeleton-driven Adaptive Hexahedral Meshing of Tubular Shapes_warrior | 287 | 77 | 262 | 254 | 88.5% | 5.99% | 82 | 28.57% |
| 2016 - Skeleton-driven Adaptive Hexahedral Meshing of Tubular Shapes_blood_vessel | 52 | 17 | 48 | 48 | 92.31% | 5.77% | 15 | 28.85% |
| 2017 - Hexahedral Mesh Generation via Constrained Quadrilateralization_cube | 17 | 5 | 16 | 13 | 76.47% | 8.7% | 5 | 29.41% |
| 2017 - Hexahedral Mesh Generation via Constrained Quadrilateralization_pone.0177603.s001 | 17 | 5 | 14 | 13 | 76.47% | 8.7% | 5 | 29.41% |
| 2012 - All-Hex Meshing using Singularity-Restricted Field_double | 71 | 19 | 52 | 41 | 57.75% | 25.25% | 21 | 29.58% |
| 2016 - Skeleton-driven Adaptive Hexahedral Meshing of Tubular Shapes_cactus | 37 | 11 | 33 | 33 | 89.19% | 8.11% | 11 | 29.73% |
| 2016 - Skeleton-driven Adaptive Hexahedral Meshing of Tubular Shapes_clef | 37 | 11 | 33 | 33 | 89.19% | 8.11% | 11 | 29.73% |
| 2016 - Skeleton-driven Adaptive Hexahedral Meshing of Tubular Shapes_dino | 47 | 14 | 47 | 47 | 100% | 0% | 14 | 29.79% |
| 2016 - Skeleton-driven Adaptive Hexahedral Meshing of Tubular Shapes_octopus | 104 | 30 | 75 | 69 | 66.35% | 9.68% | 31 | 29.81% |
| 2016 - Structured Volume Decomposition via Generalized Sweeping_hand7_3 | 67 | 20 | 46 | 40 | 59.7% | 16.38% | 20 | 29.85% |
| 2016 - Polycube simplification for coarse layouts of surfaces and volumes_hand_model_out | 107 | 32 | 74 | 70 | 65.42% | 14.33% | 32 | 29.91% |
| 2016 - Polycube simplification for coarse layouts of surfaces and volumes_hand_polycube_out | 107 | 32 | 74 | 70 | 65.42% | 14.33% | 32 | 29.91% |
| 2017 - Explicit Cylindrical Maps for General Tubular Shapes_femur_shell1 | 30 | 8 | 24 | 22 | 73.33% | 11.76% | 9 | 30% |
| 2017 - Explicit Cylindrical Maps for General Tubular Shapes_femur_shell2 | 30 | 8 | 24 | 22 | 73.33% | 11.76% | 9 | 30% |
| 2019 - Singularity Structure Simplification of Hexahedral Mesh via Weighted Ranking_toy2_output | 129 | 34 | 94 | 88 | 68.22% | 12.47% | 39 | 30.23% |
| 2019 - Selective Padding for Polycube-Based Hexahedral Meshing_Gear | 85 | 24 | 46 | 45 | 52.94% | 7.06% | 26 | 30.59% |
| 2016 - Polycube simplification for coarse layouts of surfaces and volumes_cubespikes_model_out | 111 | 28 | 107 | 101 | 90.99% | 9.35% | 34 | 30.63% |
| 2016 - Polycube simplification for coarse layouts of surfaces and volumes_cubespikes_polycube_out | 111 | 28 | 107 | 101 | 90.99% | 9.35% | 34 | 30.63% |
| 2015 - Practical Hex-Mesh Optimization via Edge-Cone Rectification_block_in | 100 | 31 | 100 | 98 | 98% | 2.08% | 31 | 31% |
| 2015 - Practical Hex-Mesh Optimization via Edge-Cone Rectification_block_out | 100 | 31 | 100 | 98 | 98% | 2.08% | 31 | 31% |
| 2015 - Practical Hex-Mesh Optimization via Edge-Cone Rectification_block_stresstest_in | 100 | 31 | 100 | 98 | 98% | 2.08% | 31 | 31% |
| 2015 - Practical Hex-Mesh Optimization via Edge-Cone Rectification_block_stresstest_out | 100 | 31 | 100 | 98 | 98% | 2.08% | 31 | 31% |
| 2016 - Structured Volume Decomposition via Generalized Sweeping_hand7_1 | 67 | 21 | 46 | 40 | 59.7% | 17.8% | 21 | 31.34% |
| 2016 - Structured Volume Decomposition via Generalized Sweeping_hand7_2 | 67 | 19 | 46 | 40 | 59.7% | 17.8% | 21 | 31.34% |
| 2016 - Polycube simplification for coarse layouts of surfaces and volumes_block_model_out | 100 | 33 | 100 | 98 | 98% | 2.08% | 33 | 33% |
| 2016 - Polycube simplification for coarse layouts of surfaces and volumes_block_polycube_out | 100 | 33 | 100 | 98 | 98% | 2.08% | 33 | 33% |
| 2019 - Symmetric Moving Frames_hex_brokenbullet | 24 | 7 | 20 | 17 | 70.83% | 12.37% | 8 | 33.33% |
| 2016 - Structured Volume Decomposition via Generalized Sweeping_kitten_with_bifur_1 | 26 | 5 | 22 | 22 | 84.62% | 10.53% | 9 | 34.62% |
| 2019 - Dual Sheet Meshing - An Interactive Approach to Robust Hexahedralization_rod | 43 | 16 | 40 | 36 | 83.72% | 8.18% | 15 | 34.88% |
| 2016 - Efficient Volumetric PolyCube-Map Construction_Sphinx_hex-f | 30 | 10 | 23 | 23 | 76.67% | 11.11% | 11 | 36.67% |
| 2016 - Skeleton-driven Adaptive Hexahedral Meshing of Tubular Shapes_fertility | 49 | 18 | 45 | 41 | 83.67% | 15.56% | 18 | 36.73% |
| 2017 - Explicit Cylindrical Maps for General Tubular Shapes_femur | 38 | 12 | 32 | 30 | 78.95% | 16.44% | 14 | 36.84% |
| 2016 - Skeleton-driven Adaptive Hexahedral Meshing of Tubular Shapes_santa | 42 | 13 | 40 | 38 | 90.48% | 8.24% | 16 | 38.1% |
| 2016 - Skeleton-driven Adaptive Hexahedral Meshing of Tubular Shapes_block | 36 | 14 | 36 | 34 | 94.44% | 5.88% | 14 | 38.89% |
| 2016 - Polycube simplification for coarse layouts of surfaces and volumes_table2_polycube_out | 59 | 19 | 58 | 53 | 89.83% | 8.62% | 23 | 38.98% |
| 2016 - Structured Volume Decomposition via Generalized Sweeping_cat_2 | 5 | 2 | 5 | 5 | 100% | 0% | 2 | 40% |
| 2016 - Structured Volume Decomposition via Generalized Sweeping_cat_3 | 5 | 2 | 5 | 5 | 100% | 0% | 2 | 40% |
| 2016 - Structured Volume Decomposition via Generalized Sweeping_Dolphin_1 | 5 | 2 | 5 | 5 | 100% | 0% | 2 | 40% |
| 2016 - Structured Volume Decomposition via Generalized Sweeping_Dolphin_2 | 5 | 2 | 5 | 5 | 100% | 0% | 2 | 40% |
| 2016 - Structured Volume Decomposition via Generalized Sweeping_Dolphin_3 | 5 | 2 | 5 | 5 | 100% | 0% | 2 | 40% |
| 2016 - Structured Volume Decomposition via Generalized Sweeping_femur1_2 | 5 | 2 | 5 | 5 | 100% | 0% | 2 | 40% |
| 2016 - Structured Volume Decomposition via Generalized Sweeping_femur1_3 | 5 | 2 | 5 | 5 | 100% | 0% | 2 | 40% |
| 2016 - Structured Volume Decomposition via Generalized Sweeping_kitten_2 | 5 | 2 | 5 | 5 | 100% | 40% | 2 | 40% |
| 2016 - Structured Volume Decomposition via Generalized Sweeping_rabbit_2 | 5 | 2 | 5 | 5 | 100% | 0% | 2 | 40% |
| 2016 - Structured Volume Decomposition via Generalized Sweeping_rabbit_3 | 5 | 2 | 5 | 5 | 100% | 0% | 2 | 40% |
| 2017 - Explicit Cylindrical Maps for General Tubular Shapes_cylinder_mixed | 7 | 3 | 7 | 7 | 100% | 0% | 3 | 42.86% |
| 2017 - Explicit Cylindrical Maps for General Tubular Shapes_cylinder_mixed_w_torsion | 7 | 3 | 7 | 7 | 100% | 0% | 3 | 42.86% |
| 2019 - Dual Sheet Meshing - An Interactive Approach to Robust Hexahedralization_bone | 16 | 6 | 12 | 12 | 75% | 4.26% | 7 | 43.75% |
| 2016 - Structured Volume Decomposition via Generalized Sweeping_bunny_1 | 18 | 8 | 16 | 16 | 88.89% | 6.74% | 8 | 44.44% |
| 2016 - Structured Volume Decomposition via Generalized Sweeping_bunny_2 | 18 | 8 | 16 | 16 | 88.89% | 6.74% | 8 | 44.44% |
| 2016 - Structured Volume Decomposition via Generalized Sweeping_bunny6_1 | 18 | 8 | 16 | 16 | 88.89% | 6.74% | 8 | 44.44% |
| 2016 - Structured Volume Decomposition via Generalized Sweeping_bunny6_2 | 18 | 8 | 16 | 16 | 88.89% | 6.74% | 8 | 44.44% |
| 2016 - Structured Volume Decomposition via Generalized Sweeping_bunny6_3 | 18 | 8 | 16 | 16 | 88.89% | 6.74% | 8 | 44.44% |
| 2019 - Selective Padding for Polycube-Based Hexahedral Meshing_Column | 18 | 8 | 18 | 17 | 94.44% | 3.85% | 8 | 44.44% |
| 2016 - All-Hex Meshing Using Closed-Form Induced Polycube_nut-hex | 12 | 6 | 12 | 12 | 100% | 0% | 6 | 50% |
| 2019 - Symmetric Moving Frames_hex_tetrahedron | 4 | 2 | 4 | 4 | 100% | 0% | 2 | 50% |
| 2017 - Explicit Cylindrical Maps for General Tubular Shapes_spring | 7 | 4 | 7 | 7 | 100% | 0% | 4 | 57.14% |
| 2016 - All-Hex Meshing Using Closed-Form Induced Polycube_fancy_ring-hex | 5 | 3 | 5 | 5 | 100% | 14.29% | 3 | 60% |
| 2016 - Structured Volume Decomposition via Generalized Sweeping_cat_1 | 5 | 3 | 5 | 5 | 100% | 0% | 3 | 60% |
| 2016 - Structured Volume Decomposition via Generalized Sweeping_femur1_1 | 5 | 3 | 5 | 5 | 100% | 0% | 3 | 60% |
| 2016 - Structured Volume Decomposition via Generalized Sweeping_kitten_1 | 5 | 3 | 5 | 5 | 100% | 40% | 3 | 60% |
| 2016 - Structured Volume Decomposition via Generalized Sweeping_rabbit_1 | 5 | 3 | 5 | 5 | 100% | 0% | 3 | 60% |
| 2019 - Dual Sheet Meshing - An Interactive Approach to Robust Hexahedralization_double-torus | 5 | 3 | 5 | 5 | 100% | 0% | 3 | 60% |
| 2017 - Explicit Cylindrical Maps for General Tubular Shapes_femur_shell0 | 8 | 5 | 8 | 8 | 100% | 0% | 5 | 62.5% |
| 2016 - All-Hex Meshing Using Closed-Form Induced Polycube_KPDloekr-hex | 2 | 2 | 2 | 2 | 100% | 38.46% | 2 | 100% |
| 2017 - Explicit Cylindrical Maps for General Tubular Shapes_cylinder_grid | 1 | 1 | 1 | 1 | 100% | 0% | 1 | 100% |
| 2017 - Explicit Cylindrical Maps for General Tubular Shapes_cylinder_polar | 1 | 1 | 1 | 1 | 100% | 0% | 1 | 100% |
| 2018 - Fuzzy clustering based pseudo-swept volume decomposition for hexahedral meshing_Example_5 | 1 | 1 | 1 | 1 | 100% | 0% | 1 | 100% |

**Table C:** *Statistics on a dataset of hexahedral meshes. Numbers of blocks in the base complex (BC), reduced base complex ($BC^-$), raw motorcycle complex (raw), reduced motorcycle complex with preserved singularity-adjacent walls ($MC^+$), fully reduced motorcycle complex (MC), percentage of arcs that are T-arcs (T).*

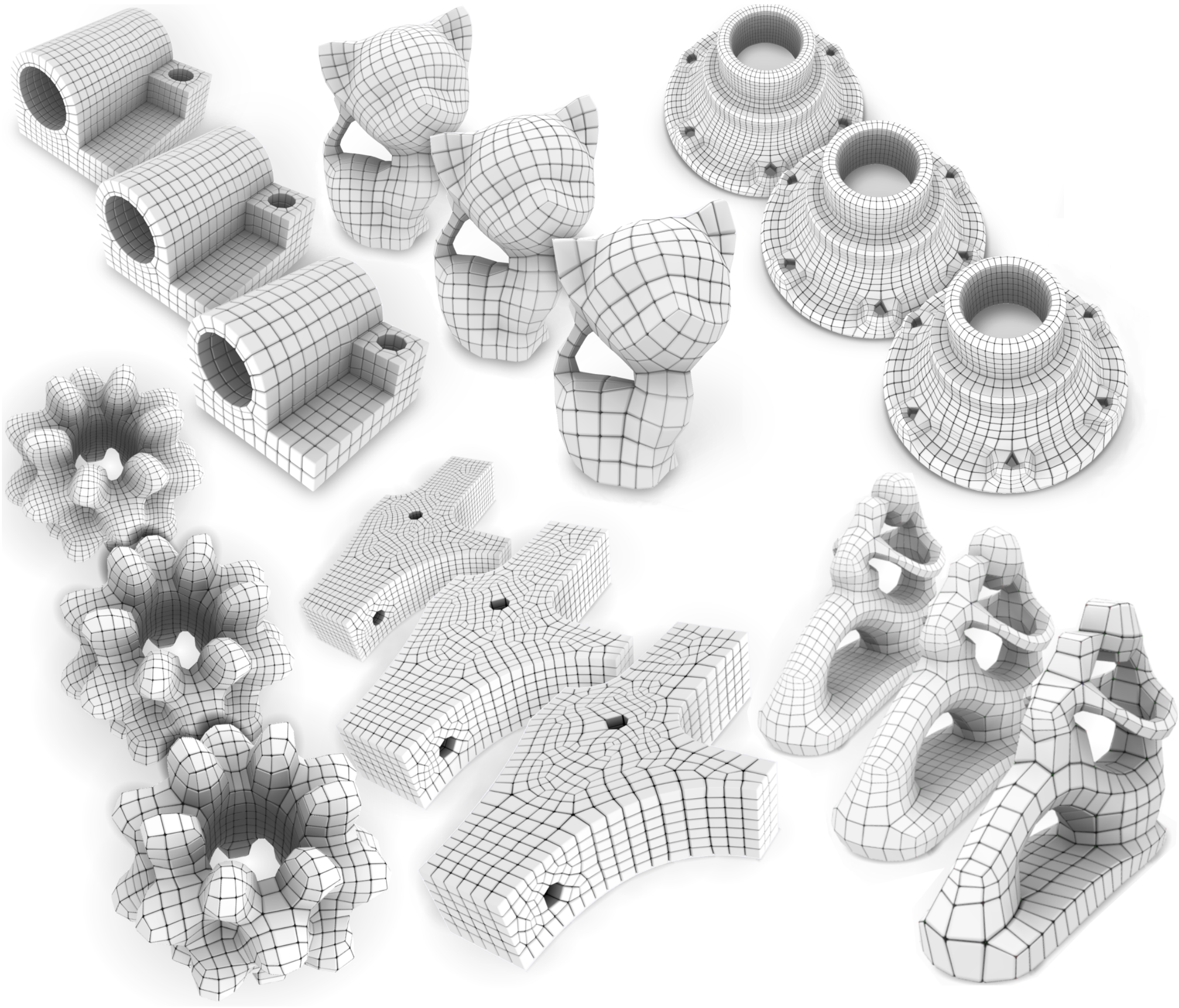

**Figure A:** *Hexahedral meshes of varying density generated by the described quantization method based on the proposed motorcycle complex.*

## D. Quantization Control

In addition to Fig. 15, Fig. A shows further examples of the ability to control the density of hexahedral meshes resulting from our quantization procedure in a fine-grained manner. To extend the range of test cases beyond those available in the dataset from Table 2 for these examples, we reconstructed seamless parametrizations from given hexahedral meshes: a tetrahedral mesh was generated, containing the singular edges, and a parametrization was imposed on it under which each hex is a unit cube. These seamlessly parametrized tetrahedral meshes can then be taken as input to the quantization procedure like those from the Table 2 dataset.

Fig. B illustrates that when basing the quantization system on the base complex rather than the motorcycle complex, density control may be significantly less fine-grained. This is intimately related to the lower number of degrees of freedom in the conforming structure of the base complex (cf. Fig. 14).

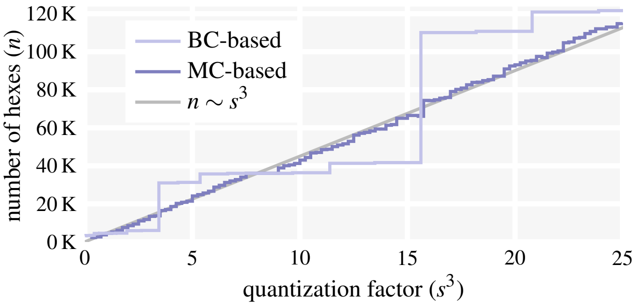

**Figure B:** *Mesh resolution can be controlled more finely when using the MC, not the BC, as basis for quantization using standard objective (10). This is illustrated here for model* EXAMPLE_2 *(Fig. A bottom center). The number of hexahedra in the extracted hex mesh is shown versus the scaling factor (i.e., target hex edge length is $1/s$). The gray line is the conceptual optimum: the number of resulting hexes exactly antiproportional to the target hex volume.*